Journal of Medical Imaging

MedicalImaging.SPIEDigitalLibrary.org

Dual-element needle transducer for intravascular ultrasound imaging

Sangpil Yoon
Min Gon Kim
Jay A. Williams
Changhan Yoon
Bong Jin Kang
Nestor Cabrera-Munoz
K. Kirk Shung
Hyung Ham Kim

SPIE.

Dual-element needle transducer for intravascular ultrasound imaging

Sangpil Yoon,[a] Min Gon Kim,[a] Jay A. Williams,[a] Changhan Yoon,[a] Bong Jin Kang,[a] Nestor Cabrera-Munoz,[a] K. Kirk Shung,[a] and Hyung Ham Kim[a,b,*]

[a]University of Southern California, Department of Biomedical Engineering, 1042 Downey Way DRB-130, Los Angeles, California 90089, United States

[b]Analogic Corporation, 8 Centennial Drive, Peabody, Massachusetts 01960, United States

Abstract. A dual-element needle transducer for intravascular ultrasound imaging has been developed. A low-frequency element and a high-frequency element were integrated into one device to obtain images which conveyed both low- and high-frequency information from a single scan. The low-frequency element with a center frequency of 48 MHz was fabricated from the single crystal form of lead magnesium niobate-lead titanate solid solution with two matching layers (MLs) and the high frequency element with a center frequency of 152 MHz was fabricated from lithium niobate with one ML. The measured axial and lateral resolutions were 27 and 122 μm, respectively, for the low-frequency element, and 14 and 40 μm, respectively, for the high-frequency element. The performance of the dual-element needle transducer was validated by imaging a tissue-mimicking phantom with lesion-mimicking area, and *ex vivo* rabbit aortas in water and rabbit whole blood. The results suggest that a low-frequency element effectively provides depth resolved images of the whole vessel and its adjacent tissue, and a high-frequency element visualizes detailed structure near the surface of the lumen wall in the presence of blood within the lumen. The advantages of a dual-element approach for intravascular imaging are also discussed. [DOI: 10.1117/1.JMI.2.2.027001]

Keywords: intravascular ultrasound imaging; dual-element needle transducer; vulnerable plaques; thin fibrous cap; lipid core; rabbit aorta; high resolution IVUS imaging without flushing.

Paper 14153R received Nov. 18, 2014; accepted for publication Mar. 24, 2015; published online Apr. 13, 2015.

1 Introduction

Vulnerable atherosclerotic plaques that are prone to rupture and lead to coronary acute events have common histopathological features. The pathological characteristics have been observed to present positive remodeling of vessel walls including a thin fibrous cap associated with a large lipid core, and macrophage infiltration through the thin fibrous cap.[1–5] The thin fibrous cap that defines vulnerable plaques has a thickness of less than 65 μm and is located near the surface of the lumen wall.[6] A large lipid core normally settles inside the arterial wall and is covered by this thin fibrous cap. Because of the structural peculiarities compared to a normal arterial wall, vulnerable plaques may be visualized by the combined use of deep penetration and high-resolution imaging strategies for detecting both the large lipid core and thin fibrous cap.

Magnetic resonance imaging[7,8] and coronary computed tomography[9,10] have been widely used for noninvasive imaging modalities to diagnose atherosclerosis. These noninvasive imaging techniques, however, do not have the capability of identifying high-risk patients by differentiating between vulnerable and stable plaques. Catheter-based techniques have been developed, such as intravascular ultrasound (IVUS), and were typically used to visualize the internal structure of coronary arteries.[11–13] Compared to a conventional single-frequency IVUS, which typically uses a center frequency between 20 and 40 MHz with a resolution of 100 to 300 μm,[13,14] the low-frequency and high-frequency dual-element imaging approaches make it possible to acquire a deep penetration depth image of the whole vessel and a higher resolution image of vessel anatomy close to the catheter at the same time.[15,16]

Intravascular optical coherence tomography (IOCT) has been introduced to characterize plaque vulnerability with high-resolution imaging capability (10 to 40 μm) at the expense of penetration depth.[17–19] Combined IVUS and IOCT imaging has been developed to increase the diagnostic accuracy of vulnerable plaques.[20,21] The most challenging part of IOCT imaging, however, is that blood needs to be cleared from the lumen since it significantly absorbs and scatters the light.[22] Clearing blood from the lumen can be achieved by vessel occlusion and/or flushing via a guide catheter.[22–25] The issues with blood clearing are that it significantly limits imaging time, which prevents the acquisition of long arterial walls, and incomplete blood clearing may unexpectedly degrade image quality.[26–28] Occlusion may also induce other side effects such as hemodynamic instability and arrhythmias.[23] The dual-element IVUS approach requires neither blood clearing from the lumen nor significant modification of an imaging system.

In this paper, we have proposed and developed a dual-element needle transducer by combining low- and high-frequency elements for IVUS imaging to achieve deep penetration depth and high resolution at the same time. Separately fabricated acoustic stacks for low- and high-frequency elements were assembled into a needle to form a dual-element needle

*Address all correspondence to: Hyung Ham Kim, E-mail: dkim@analogic.com

2329-4302/2015/$25.00

transducer. Pulse-echo response and resolution tests were performed to characterize the performance of both elements of the transducer. Images of tissue-mimicking phantoms and *ex vivo* rabbit aortas in water and in rabbit blood, using the newly developed dual-element needle transducer, were obtained and analyzed.

2 Materials and Methods

2.1 *Tissue-Mimicking Phantom and Rabbit Aorta Preparation*

Tissue-mimicking phantoms, containing 9% by weight gelatin (300-g bloom, type A, Sigma-Aldrich, Inc., St. Louis, Missouri), 1% by weight 5-μm silica particles (Min-U-Sil 5, Mill Creek, Ohio), and 1% by weight 40-μm silica particles (Min-U-Sil 40, Mill Creek, Ohio), were made [Fig. 1(a)]. When making the tissue-mimicking phantoms, a hollow rod with 5-mm outer diameter was positioned in the middle of a cuvette before the gelatin and silica mixture was poured into the cuvette to mimic the lumen of an aorta. To solidify the gelatin and silica mixture, the cuvette was then placed in the refrigerator for an hour. After removing the hollow rod from the hardened tissue-mimicking phantom, in order to create a lesion-mimicking area at the surface of the lumen wall, small gaps, which are denoted as three thick lines in Fig. 1(a), were intentionally made by cutting the surface of the lumen with a razor blade. Normal New Zealand white rabbit aortas (NRAs) with fatty tissue and rabbit blood with ethylenediaminetetraacetic acid were obtained from Sierra for Medical Science, Inc. (Whittier, California). Fatty tissue, which covered the aorta, was not removed. After a rabbit aorta was placed in the middle of the cuvette, a 9% by weight gelatin solution was poured to fill the cuvette, which was then placed inside the refrigerator for an hour. The solidified gelatin block fixed the rabbit aorta throughout the experiments to stabilize it for imaging. AXD and LTD in Fig. 1(b) stand for axial and lateral directions in polar coordinates, respectively.

2.2 *Fabrication of a Dual-Element Needle Transducer*

The acoustic stack for the low-frequency element of the needle transducer was composed of two matching layers [MLs in Fig. 2(a)], a piezoelectric material [PM in Fig. 2(a)], and a backing layer [BL in Fig. 2(a)]. The single crystal form of lead magnesium niobate-lead titanate solid solution (PMN-PT, IBULE Photonics, Incheon, Republic of Korea) was used as a PM with a thickness of 40 μm and an aperture size of 0.57×0.57 mm^2. The mixture of Insulcast 501 epoxy (American Safety Technologies, Roseland, New Jersey) and 2- to 3-μm silver particles (Aldrich Chemical Co., Milwaukee, Wisconsin) was cast over the PM to form an inner, or first, ML with a final thickness of 10 μm. A conductive silver epoxy (E-Solder 3022, Von Roll Isola Inc., New Haven, Connecticut) was molded on the back side of the PM to form a BL. The thickness of the BL was approximately 1 mm. The second ML was formed at the end of the fabrication process on top of the inner, or first, ML.

The acoustic stack of the high-frequency element comprised one ML, a PM, and a BL [see Fig. 2(a)]. Two 36-deg-rotated Y-cut lithium niobate plates ($LiNbO_3$, Boston Piezo-Optics, Bellingham, Massachusetts) were lapped down to the desired thickness of 15 μm. A conductive silver epoxy was cast on one side of the PM to form a BL with a thickness of approximately 1 mm. The aperture of the high-frequency element acoustic stack was also 0.57×0.57 mm^2. The ML was applied at the end of the fabrication process on top of the PM.

The high-frequency element [HE in Fig. 2(b)] and low-frequency element [LE in Fig. 2(b)] acoustic stacks were press-focused with a stainless steel ball of 5-mm diameter to make a focal point at approximately 2.5 mm. The f-number of both elements was approximately 4.3. An elliptical hole was made at the distal end of a stainless steel hypodermic needle with inner and outer diameters of approximately 0.9 and 1.06 mm, respectively. A silver wire with a thin insulating jacket was connected to the BL of each acoustic stack using a conductive silver epoxy. HE and LE acoustic stacks with silver wires attached were

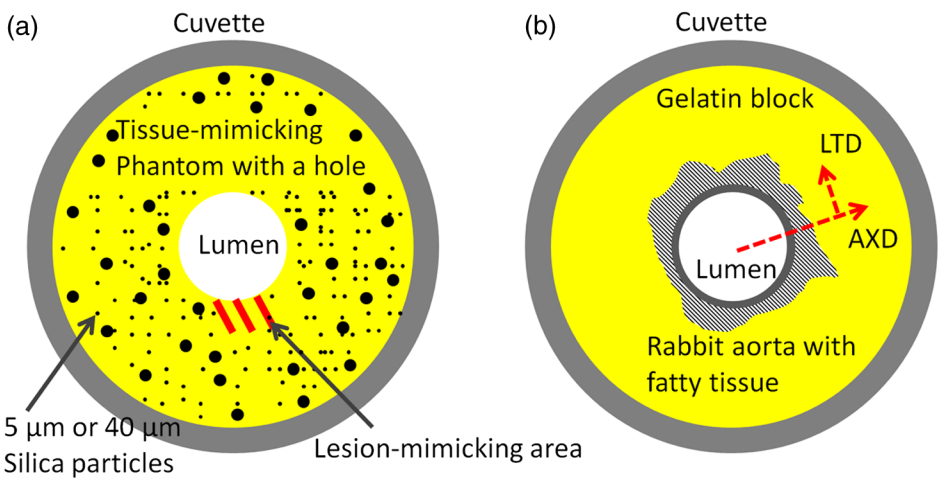

Fig. 1 Schematic diagram of tissue-mimicking phantom and rabbit aorta specimen for imaging. (a) Tissue-mimicking phantom, containing 9% by weight gelatin, 1% by weight 5-μm silica particles, and 1% by weight 40-μm silica particles, was placed in a cuvette with a lumen in the middle of the phantom. Lesion-mimicking area was made (thick solid lines) by cutting the surface of lumen. (b) Rabbit aorta specimen with fatty tissue (hatched area) was fixed by 9% by weight gelatin without scatterers to stabilize the specimen for imaging. AXD and LTD stand for axial and lateral directions, respectively.

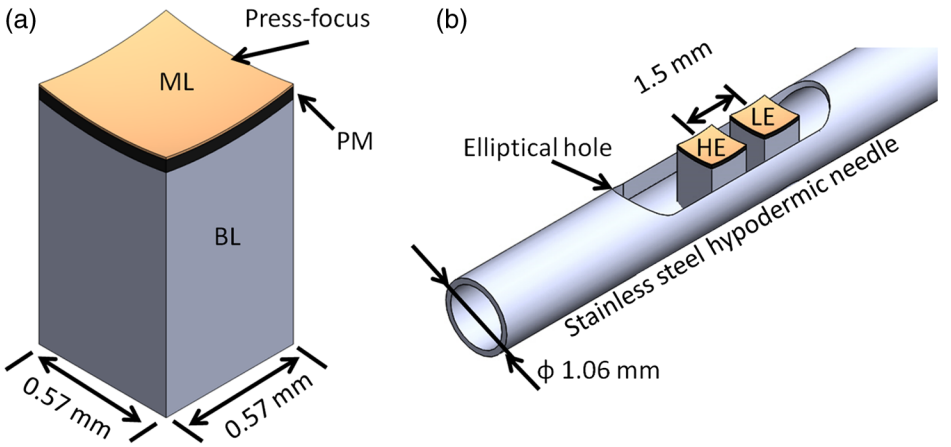

Fig. 2 (a) Press-focused acoustic stacks for a low-frequency element and a high-frequency element are composed of one or two matching layers (MLs) on top of piezoelectric materials (PMs) followed by backing layer (BL). The focus of an acoustic stack was at approximately 2.5 mm and the size of an acoustic stack was 0.57×0.57 mm^2. (b) Fabricated acoustic stacks for low-frequency element (LE) and high-frequency element (HE) were integrated in series within the stainless steel hypodermic needle with the outer diameter of 1.06 mm. The center-to-center distance between LE and HE was 1.5 mm.

placed side by side in the elliptical hole at the distal end of the stainless steel hypodermic needle. The center-to-center distance between HE and LE was 1.5 mm. The gaps between the acoustic stacks and the stainless tubing were filled in with an insulating epoxy (Epo-Tek 301, Epoxy Technologies, Billerica, Massachusetts).

The whole area of the distal end of the stainless steel needle, including the low- and high-frequency elements, was sputtered with a chrome/gold electrode at a thickness of approximately 150 nm to make a ground connection between the acoustic stacks and the stainless steel hypodermic needle. The silver wires from the low- and high-frequency elements were connected to two separate SMA connectors. As the last step in the fabrication process, using a PDS 2010 Labcoater (Specialty Coating Systems, Indianapolis, Indiana), parylene was deposited on top of the inner, or first, ML of the low-frequency element as the second ML and on the lithium niobate PM of the high-frequency element as a single ML. The thicknesses of parylene MLs of the low- and high-frequency elements were 3 and 1.5 μm, respectively.

2.3 *Transducer Characterization*

Pulse-echo response and spatial resolution of the developed dual-element needle transducer were measured using an ultrasound biomicroscopy (UBM) system. The UBM system was composed of a main computer, a one-channel analog-to-digital acquisition card (A/D card, CS122G1, DynamicsSignals LLC., Lockport, Illinois), a three-dimensional (3-D) translation stage (ILS100HA, Newport, Irvine, California) with controller (ESP301-3N, Newport, Irvine, California), and a pulser/receiver (5910PR, Panametrics, Waltham, Massachusetts). The reliable minimum increment motion of the 3-D translation stage of the UBM system was 0.3 μm. A quartz block was used as a reflecting target for pulse-echo measurements at the focus of the low- and high-frequency elements. Time domain echo waveforms and their frequency spectra were estimated. The center frequency (f_c) and the -6 dB bandwidth (BW) were determined by

$$f_c = \frac{f_1 + f_2}{2},$$

$$\mathrm{BW} = \frac{f_2 - f_1}{f_c} \times 100,$$

where f_1 and f_2 are -6 dB cut-off frequencies from the estimated spectra. The dual-element needle transducer was mounted on a 3-D translation stage of a UBM system and translated with a step size of 1 μm to acquire scan lines to obtain two-dimensional (2-D) cross-sectional images of tungsten wire targets. The tungsten wire targets with diameters of 20 and 4 μm were used for resolution characterization of the low- and high-frequency elements. The point spread function (PSF) at the focus of each element was plotted along the axial and lateral directions from the 2-D cross-sectional images of tungsten wire targets to measure the axial and lateral resolutions. The axial and lateral resolutions were then determined by using the -6 dB points on the PSF plots.

2.4 *Experimental Setup and Signal Processing*

An imaging system was developed to image tissue-mimicking phantoms and rabbit aortas with fatty tissue, which were filled with water or rabbit blood (Fig. 3). The developed dual-element needle transducer was attached to a 3-D translation stage to control the position of the transducer. The cuvette, containing phantom or aorta, was placed on top of the stepper motor (Zaber Technologies, Inc., Vancouver, British Columbia, Canada) and was rotated to acquire 2564 scan lines during a 360-deg turn as shown in Fig. 3. Water or rabbit blood was injected inside the lumen (Figs. 1 and 3). The dual-element needle transducer was connected to the pulser/receiver, which was controlled by a function generator (Agilent 33250A, Agilent, Loveland, Colorado). The sequence among the function generator, the stepper motor, and the A/D card was controlled by a custom-built LabVIEW (National Instruments, Austin, Texas) program. Once the stepper motor rotated the cuvette by one increment ($360 \text{ deg}/2564 \text{ scanlines} = 0.14 \text{ deg}/\text{each scanline}$), the cuvette was stationary for 10 ms to acquire one scan line. At

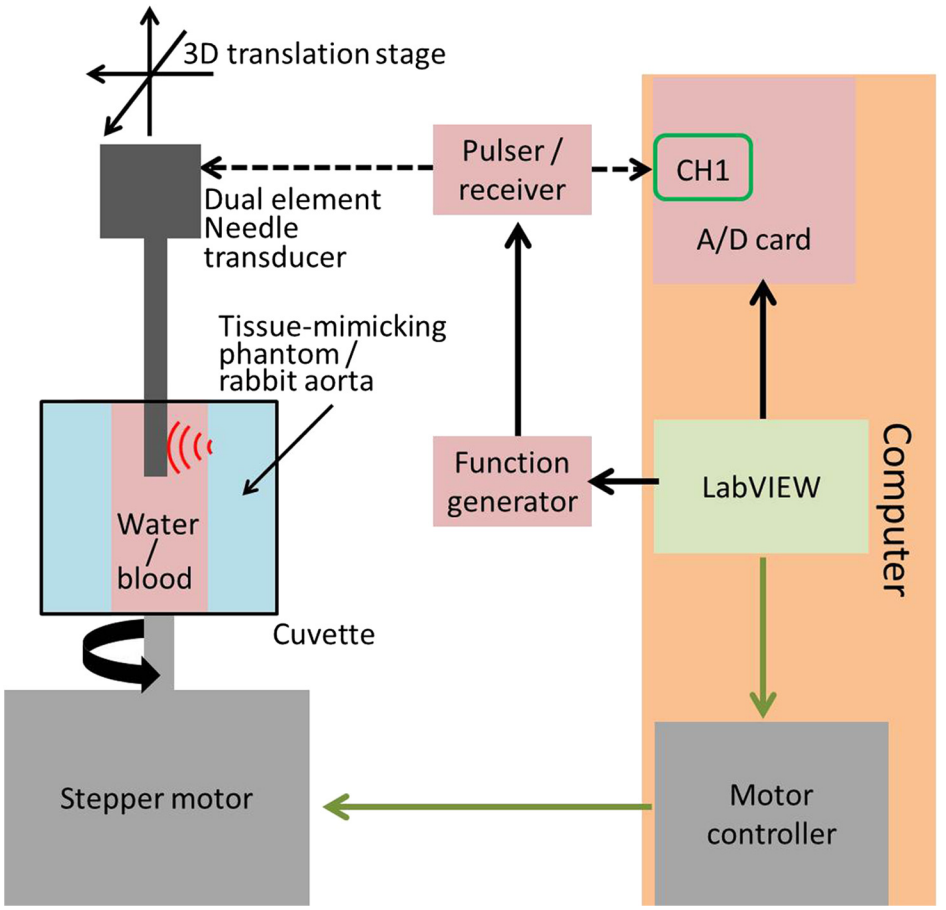

Fig. 3 A schematic view of the experimental setup. Tissue-mimicking phantom or rabbit aorta, which was filled with water or rabbit blood, was located in a cuvette. A dual-element needle transducer was attached to a three-dimensional translation stage. A stepper motor rotated the cuvette, which was coaxially aligned with the dual-element needle transducer and was stationary for 10 ms to acquire one scan line. During a 360-deg turn of the cuvette, 2564 scan lines were acquired and each scan line was composed of 8200 samples which corresponded to approximately 4.1 μs along the axial direction.

the same time, the function generator triggered the pulser/receiver and the A/D card received a trigger signal from the pulser/receiver. The pulser/receiver triggered the dual-element needle transducer to emit a pulse and to receive backscattered ultrasound echoes. Radio frequency (RF) raw data of the emitted pulses and backscattered ultrasound echoes were digitized by the A/D card with a sampling rate of 1 GHz and saved at computer storage from channel 1 of the A/D card for offline processing. Each scan line had 8200 samples, which corresponded to a 4.1 μs in the axial direction [AXD in Fig. 1(b)]. The 26 and 40 dB gains were applied to the received RF raw data of the low- and high-frequency elements, respectively. After one imaging plane was obtained by the low-frequency element, the transducer was moved up by 1.5 mm to image the same plane with the high-frequency element.

The stored RF raw data for each element were high-pass filtered to remove the DC offset and were then used to construct scan-converted images of the tissue-mimicking phantom or rabbit aorta. Quadrature demodulation was used to baseband the RF raw data followed by a low-pass filter with the cut-off frequency of $0.5 \times f_c \times \mathrm{BW}/100$ MHz. The scan conversion of R-theta data was performed to transform polar coordinates to rectangular coordinates. Bilinear interpolation was also applied to construct cross-sectional images of the tissue-mimicking phantoms and aortas.

3 Results

3.1 *Pulse-Echo Response and Resolution of Dual-Element Needle Transducer*

Time domain pulse-echo waveforms and their spectra of the low- and high-frequency elements are presented, as shown in Fig. 4. The measured center frequency (f_c) and -6 dB BW of the low-frequency element of the dual-element needle transducer were 48 MHz and 86%, respectively [Figs. 4(a) and 4(b)]. The measured f_c and -6 dB BW of the high-frequency element were 152 MHz and 28% [Figs. 4(c) and 4(d)].

Two-dimensional cross-sectional images of 20- and 4-μm tungsten wires obtained by the low- and high-frequency elements of the dual-element needle transducer are shown in Figs. 5(a) and 5(d). Axial and lateral beam profiles of 2-D cross-sectional images of the low- and high-frequency elements are presented, as shown in Figs. 5(b), 5(c) and 5(e), 5(f). The measured axial and lateral resolutions of the low-frequency element were 27 and 122 μm using the -6 dB widths in Figs. 5(b) and 5(c). The measured axial and lateral resolutions

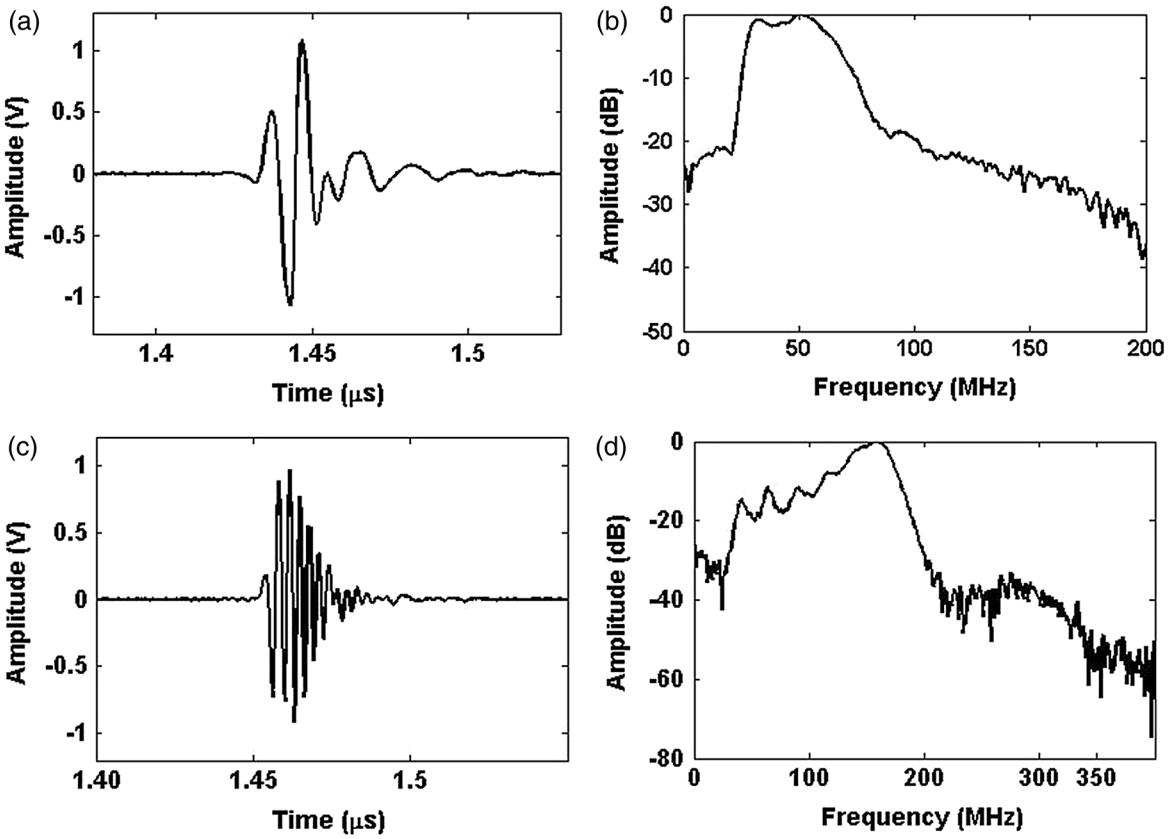

Fig. 4 (a) Time domain pulse-echo waveform and (b) its spectrum of the low-frequency element. The center frequency and the −6 dB bandwidth (BW) were estimated as 48 MHz and 86%. (c) Time domain pulse-echo waveform and (d) its spectrum of the high-frequency element. The center frequency and the BW of the high-frequency element were measured as 152 MHz and 28%, respectively.

of the high-frequency element were 14 and 40 μm [Figs. 5(e) and 5(f)].

3.2 *Imaging of Tissue-Mimicking Phantom and Ex Vivo Rabbit Aorta*

Figures 6(a) and 6(b) show the images of a tissue-mimicking phantom obtained by the low- and high-frequency elements of the dual-element needle transducer, respectively. The dynamic ranges of Figs. 6(a) and 6(b) are 60 and 30 dB, respectively. Figure 6(c) shows the combined image of the images in Figs. 6(a) and 6(b), which demonstrates the high-resolution imaging capability near the lumen wall while the deep region is also visualized. Three solid arrows in Figs. 6(a) and 6(b) indicate the lesion-mimicking area [solid lines in Fig. 1(a)]. The image obtained by the low-frequency element is not able to show the lesions-mimicking area [Fig. 6(a)]; however, the image obtained by the high-frequency element clearly shows the artificial lesions as shown in Fig. 6(b).

The cross-sectional images of a normal NRA, which is filled with water, are presented. Figures 7(a) and 7(b) show NRA images obtained by the low- and high-frequency elements. Solid and dashed arrows in Fig. 7(a) indicate the NRA and surrounding fatty tissue, respectively. The boundary between water and NRA and NRA and fatty tissue are clearly distinguished as shown in Fig. 7(a). The image in Fig. 7(b) visualizes the surface of the lumen wall with high resolution at the expense of penetration depth. The dynamic ranges of Figs. 7(a) and 7(b) are 60 and 30 dB, respectively.

Figure 8 demonstrates images of a normal NRA with the presence of rabbit whole blood in the lumen. Figure 8(a), which was obtained by the low-frequency element of the dual-element needle transducer, presents the clear boundary among rabbit blood, NRA [solid arrow in Fig. 8(a)], and fatty tissue [dashed arrow in Fig. 8(a)]. The image of the same cross section of the NRA, obtained by the high-frequency element, is shown in Fig. 8(b). The surface of the lumen wall of the NRA is clearly shown in Fig. 8(b) with high resolution and is distinguishable from the scattering caused by the rabbit blood. Scattering from rabbit blood exists in the lumen of NRA as shown in Figs. 8(a) and 8(b). Figure 8(c) shows the combined image of Figs. 8(a) and 8(b). The dynamic ranges of Figs. 8(a) and 8(b) are 60 and 30 dB, respectively.

4 Discussion

To evaluate the performance of low- and high-frequency elements of a dual-element needle transducer, corresponding image pairs were constructed and compared. High-frequency element images provided detailed morphologic information as shown in Figs. 6(b), 7(b), and 8(b), which may be used to improve the detection of a thin fibrous cap (<65 μm), thought to be one of the main pathological features of vulnerable plaques. The high-resolution image also facilitated the identification of the lesion-mimicking area, indicated by solid lines in Fig. 1(a) and arrows in Fig. 6(b). The same region could not be discerned by the low-frequency element as shown in Fig. 6(a). On the other hand, low-frequency images visualized

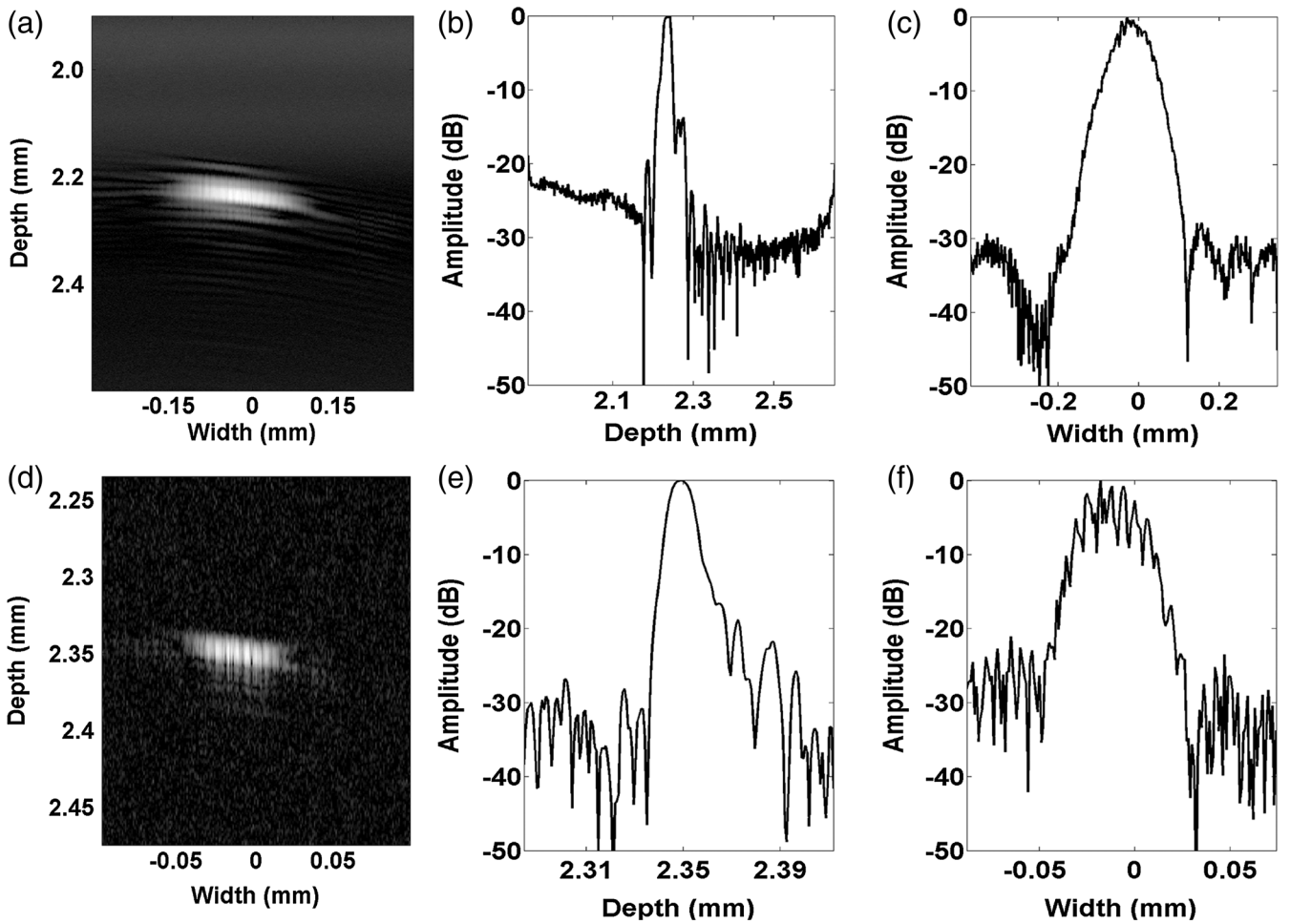

Fig. 5 (b) Axial and (c) lateral beam profiles of the low-frequency element obtained from (a) the two-dimensional (2-D) cross-sectional image of a 20-μm tungsten wire target. Measured axial and lateral resolutions were 27 and 122 μm. (e) Axial and (f) lateral beam profiles from (d) the 2-D cross-sectional image of a 4-μm tungsten wire target obtained from the high-frequency element. The axial and lateral resolutions were measured as 14 and 40 μm, respectively.

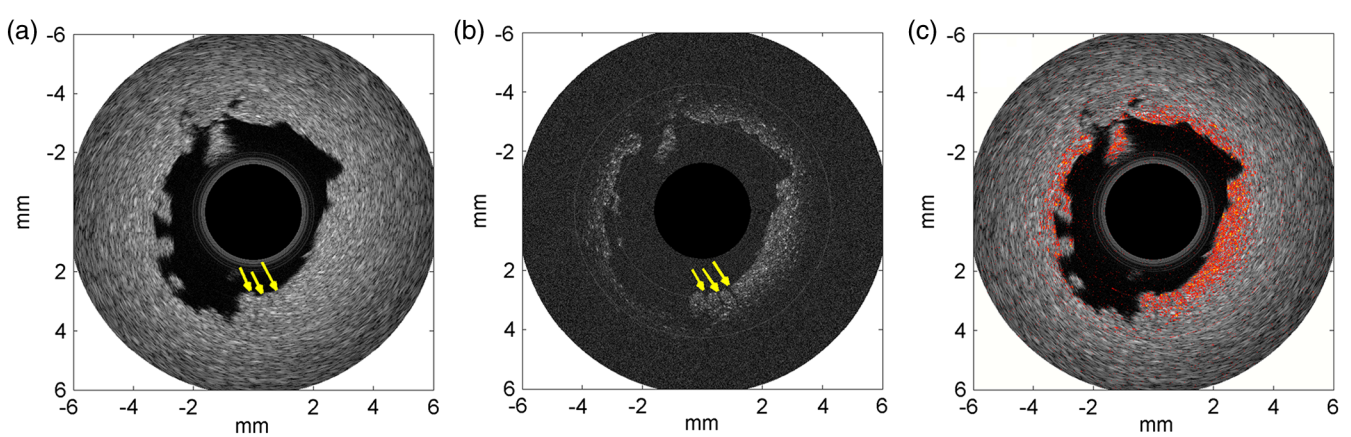

Fig. 6 Tissue-mimicking phantom images obtained by (a) the low-frequency element and (b) the high-frequency element of a dual-element needle transducer are shown. (c) Combined images of (a) and (b) are also shown in one axis with the normal gray-scaled image of (a) and a red-scaled image of (b). Solid arrows in (a) and (b) indicate the artificially created lesion-mimicking area on the surface of a lumen wall. In image (b), which is obtained by the high-frequency element, artificially created lesions are clearly visualized.

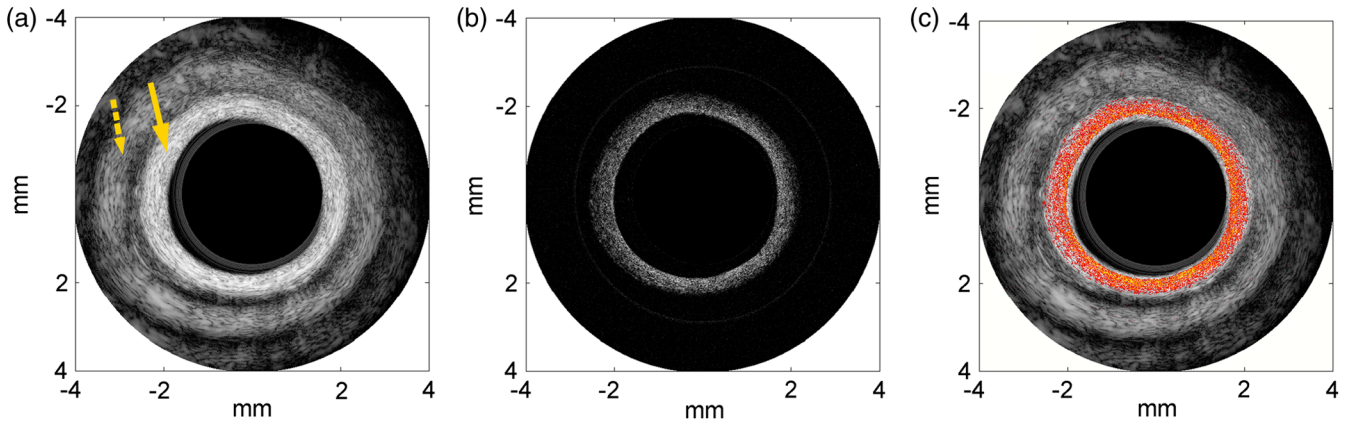

Fig. 7 Normal *ex vivo* rabbit aorta images obtained by (a) the low-frequency element and (b) the high-frequency element of a dual-element needle transducer in water. In (a), the solid arrow indicates the rabbit aorta and the dashed arrow indicates fatty tissue. Water, rabbit aorta, and fatty tissues are clearly distinguished in (a). High-resolution image visualizes surface near the lumen wall of the rabbit aorta in (b). (c) Combined image is shown with the gray-scaled image of (a) and a red-scaled image of (b).

the fatty tissues surrounding the aorta as well as the entire lumen wall, indicated as dashed and solid arrows in Figs. 7(a) and 8(a). Even though the lumen of the aorta was filled with whole rabbit blood, the lumen wall and surrounding fatty tissues were clearly distinguishable as shown in Fig. 8(a). Due to the greater tissue penetration of low-frequency ultrasound, the low-frequency element was able to provide complementary information on vessel remodeling that was not available from the high-frequency element.

In this paper, the high-frequency element with a center frequency of 152 MHz and f-number of 4.3 had a lateral resolution of approximately 40 μm, which is comparable to that of OCT.[14] The high-frequency element had 28% −6 dB BW [Fig. 4(d)], which seems to be a relatively low fractional BW. Low −6 dB BW resulted in coarse axial resolution, which limited the diagnostic capabilities of the high-frequency element.[29] However, the absolute BW of the high-frequency element is still large compared to typical low-frequency transducers. Absolute BW of the high-frequency element was approximately 43 MHz, which corresponds to the 100% fractional BW of a transducer with a center frequency of 43 MHz. Therefore, the high-frequency element has the capability to resolve fine structures in the axial direction as well as the lateral direction due to superior axial and lateral resolutions of 14 and 40 μm, respectively.

The high-frequency element has the capability to delineate the presence of the thin fibrous cap because the high-frequency element has a higher spatial resolution compared to the thickness of the thin fibrous cap, which is normally less than 65 μm.[6] The thin fibrous cap will be recognized as a much brighter region in IVUS images than other plaque components if the high-frequency is used.[30,31] High frequency induces stronger scattering than low frequency does and fibrous tissue, which forms the thin fibrous cap, generates more increased echogenicity than other plaque components such as the necrotic core does.

To further increase the axial resolution of the high-frequency element, a two ML scheme, similar to the low-frequency

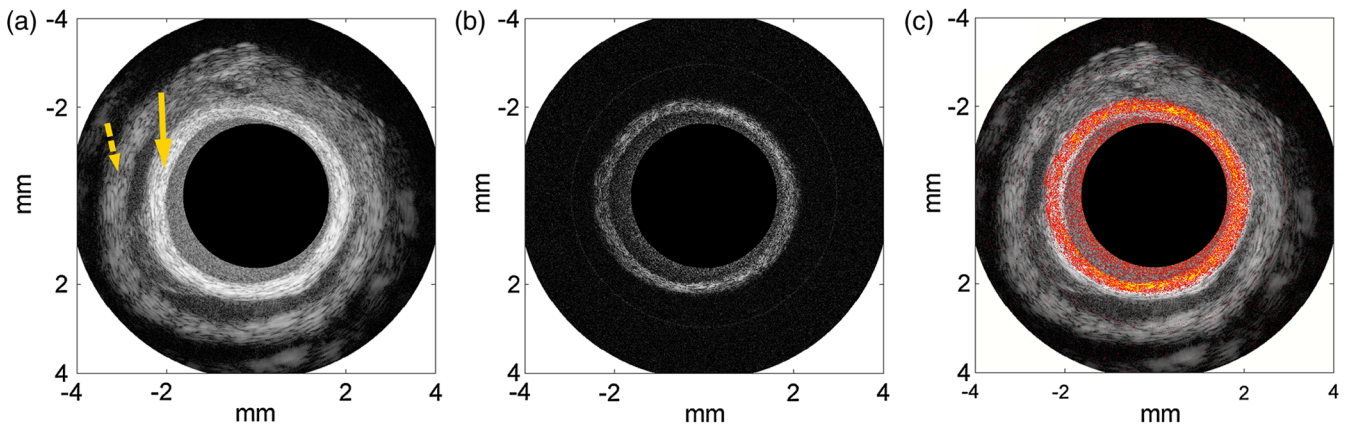

Fig. 8 Normal *ex vivo* rabbit aorta images, acquired by (a) low-frequency element and (b) high-frequency element, are shown with the presence of rabbit whole blood in the lumen. (c) The combined image of (a) and (b) is shown with the gray-scaled image of (a) and a red-scaled image of (b). Scattering from blood inside the lumen is clearly visible in all images. Three different layers such as blood, aorta, and fatty tissue are clearly distinguished in (a). The image in (b) delineates the surface of the aorta wall with high resolution with the presence of whole blood in the lumen.

element, may be used.[32] Alternatively, electrical matching of the transducer may also be used to increase axial resolution. Besides −6 dB BW, sensitivity was also an important factor for transducers with such a small aperture size. To increase the sensitivity of transducers, both elements were press-focused. Compared to unfocused transducers, focused transducers are able to deliver much more energy at the point of interest. Focusing increased the energy near the lumen wall to acquire high-resolution images, particularly for the high-frequency element, which had to image micrometer-sized structures, such as the thin fibrous cap. The focal distance of approximately 2.5 mm was chosen after considering the fact that the typical inner diameter of the human coronary artery is usually less than 4.5 mm.[33]

Images of normal rabbit aortas did not present significant morphological abnormalities that come from a diseased artery. In this paper, only normal rabbit aortas were imaged because of the difficulty in acquiring an animal specimen with atherosclerosis-related disease.[34] Because the validation of a dual-element needle transducer has been confirmed, the imaging of a diseased coronary artery will be performed as future work.

The outer diameter of the current dual-element needle transducer was 1.06 mm. For future applications, the outer diameter should be smaller than 0.7 mm in order to place the transducer inside the catheter sheath in which it rotates for successful translation to clinical use. In conjunction with the size of the transducer, coregistration of two elements may also pose a problem. In this paper, two individual elements were linearly aligned with a 1.5 mm center-to-center distance and images obtained by the two elements were manually compared until similar pairs were acquired. From the image coregistration point of view, concentric focusing, which shares the same focal point, was the best solution; however, concentrically focused elements are usually too large to be used in IVUS catheters. Three-dimensional reconstruction of the coronary artery with the low-frequency and high-frequency information from one scan promises to improve the understanding of vessel and plaque pathology. Three-dimensional reconstruction may enhance the histophathologic function of dual-element IVUS by visualizing the precise architecture of coronary arteries.

5 Conclusions

We have developed a dual-element needle transducer for IVUS imaging. Two separate acoustic stacks for a low-frequency element and a high-frequency element were integrated into one transducer. The developed dual-element needle transducer successfully provided images of tissue-mimicking phantoms and *ex vivo* rabbit aortas in water or with the presence of blood with high resolution and deep penetration.

Acknowledgments

This work was supported by the International Collaborative R&D Program (No. 1150049) funded by the Ministry of Trade, Industry, and Energy (MOTIE), Republic of Korea [No. 1150049, developing high frequency bandwidth (40 to 60 MHz) high-resolution image system and probe technology for diagnosing cardiovascular lesion]. This work was also supported in part by the National Institutes of Health under Grant No. P41-EB002182.

References

1. S. Glagov et al., "Compensatory enlargement of human atherosclerotic coronary arteries," *N. Engl. J. Med.* **316**(22), 1371–1375 (1987).
2. R. T. Lee and P. Libby, "The unstable atheroma," *Arterioscler. Thromb. Vasc. Biol.* **17**(10), 1859–1867 (1997).
3. A. M. Varnava, P. G. Mills, and M. J. Davies, "Relationship between coronary artery remodeling and plaque vulnerability," *Circulation* **105**(8), 939–943 (2002).
4. M. Naghavi et al., "From vulnerable plaque to vulnerable patient–Part III: executive summary of the screening for heart attack prevention and education (SHAPE) task force report," *Am. J. Cardiol.* **98**(2A), 2H–15H (2006).
5. V. E. Friedewald et al., "The editor's roundtable: atherosclerosis regression," *Am. J. Cardiol.* **101**(7), 967–974 (2008).
6. R. Virmani et al., "Lessons from sudden coronary death: a comprehensive morphological classification scheme for atherosclerotic lesions," *Arterioscler. Thromb. Vasc. Biol.* **20**(5), 1262–1275 (2000).
7. J. F. Toussaint et al., "Magnetic resonance images lipid, fibrous, calcified, hemorrhagic, and thrombotic components of human atherosclerosis in vivo," *Circulation* **94**(5), 932–938 (1996).
8. G. Helft et al., "Progression and regression of atherosclerotic lesions: monitoring with serial noninvasive magnetic resonance imaging," *Circulation* **105**(8), 993–998 (2002).
9. M. J. Budoff and B. H. Brundage, "Electron beam computed tomography: screening for coronary artery disease," *Clin. Cardiol.* **22**(9), 554–558 (1999).
10. M. Naghavi et al., "New developments in the detection of vulnerable plaque," *Curr. Atheroscler. Rep.* **3**(2), 125–135 (2001).
11. G. S. Mintz et al., "American College of Cardiology clinical expert consensus document on standards for acquisition, measurement and reporting of intravascular ultrasound studies (IVUS). A report of the American College of Cardiology Task Force on clinical expert consensus documents," *J. Am. Coll. Cardiol.* **37**(5), 1478–1492 (2001).
12. H. M. Garcia-Garcia, M. A. Costa, and P. W. Serruys, "Imaging of coronary atherosclerosis: intravascular ultrasound," *Eur. Heart J.* **31**(20), 2456–2469 (2010).
13. S. Yoon et al., "Angled-focused 45 MHz PMN-PT single element transducer for intravascular ultrasound imaging," *Sensor Actuat. A-Phys.* **228**, 16–22 (2015).
14. K. Jansen, G. van Soest, and A. F. van der Steen, "Intravascular photoacoustic imaging: a new tool for vulnerable plaque identification," *Ultrasound Med. Biol.* **40**(6), 1037–1048 (2014).
15. C. E. Munding et al., "Multifrequency intravascular ultrasound for assessment of atherosclerotic plaque vulnerability," in *Abstract in IEEE Int. Ultrasonics Symp.*, pp. 132–133 (2013).
16. T. Ma et al., "Multi-frequency intravascular ultrasound (IVUS) imaging," *IEEE Trans. Ultrasonics Ferroelectr. Freq. Control* **62**(1), 97–107 (2015).
17. M. E. Brezinski et al., "Optical coherence tomography for optical biopsy. Properties and demonstration of vascular pathology," *Circulation* **93**(6), 1206–1213 (1996).
18. I. K. Jang et al., "Visualization of coronary atherosclerotic plaques in patients using optical coherence tomography: comparison with intravascular ultrasound," *J. Am. Coll. Cardiol.* **39**(4), 604–609 (2002).
19. G. Guagliumi and V. Sirbu, "Optical coherence tomography: high resolution intravascular imaging to evaluate vascular healing after coronary stenting," *Catheter. Cardiovasc. Interventions* **72**(2), 237–247 (2008).
20. X. Li et al., "Integrated IVUS-OCT imaging for atherosclerotic plaque characterization," *IEEE J. Sel. Top. Quantum Electron.* **20**(2), 7100108 (2014).
21. B. H. Li et al., "Hybrid intravascular ultrasound and optical coherence tomography catheter for imaging of coronary atherosclerosis," *Catheter. Cardiovasc. Interventions* **81**(3), 494–507 (2013).
22. T. Yamaguchi et al., "Safety and feasibility of an intravascular optical coherence tomography image wire system in the clinical setting," *J. Am. Coll. Cardiol.* **101**(5), 562–567 (2008).
23. J. Tanigawa, P. Barlis, and C. Di Mario, "Intravascular optical coherence tomography: optimisation of image acquisition and quantitative assessment of stent strut apposition," *EuroIntervention* **3**(1), 128–136 (2007).
24. F. Prati et al., "Expert review document on methodology, terminology, and clinical applications of optical coherence tomography: physical principles, methodology of image acquisition, and clinical application for assessment of coronary arteries and atherosclerosis," *Eur. Heart J.* **31**(4), 401–415 (2010).

25. H. Kataiwa et al., "Head to head comparison between the conventional balloon occlusion method and the non-occlusion method for optical coherence tomography," *Int. J. Cardiol.* **146**(2), 186–190 (2011).
26. I. K. Jang, G. Tearney, and B. Bouma, "Visualization of tissue prolapse between coronary stent struts by optical coherence tomography: comparison with intravascular ultrasound," *Circulation* **104**(22), 2754 (2001).
27. I. K. Jang et al., "In vivo characterization of coronary atherosclerotic plaque by use of optical coherence tomography," *Circulation* **111**(12), 1551–1555 (2005).
28. M. Brezinski et al., "Index matching to improve optical coherence tomography imaging through blood," *Circulation* **103**(15), 1999–2003 (2001).
29. F. S. Foster et al., "Advances in ultrasound biomicroscopy," *Ultrasound Med. Biol.* **26**(1), 1–27 (2000).
30. R. Yamada et al., "Relationship between arterial and fibrous cap remodeling: a serial three-vessel intravascular ultrasound and optical coherence tomography study," *Circ. Cardiovasc. Interventions* **3**(5), 484–490 (2010).
31. D. Stamper, N. J. Weissman, and M. Brezinski, "Plaque characterization with optical coherence tomography," *J. Am. Coll. Cardiol.* **47**(8), C69–C79 (2006).
32. Q. Zhou et al., "Piezoelectric films for high frequency ultrasonic transducers in biomedical applications," *Prog. Mater. Sci.* **56**(2), 139–174 (2011).
33. J. T. Dodge, Jr. et al., "Lumen diameter of normal human coronary arteries. Influence of age, sex, anatomic variation, and left ventricular hypertrophy or dilation," *Circulation* **86**(1), 232–246 (1992).
34. J. A. Piedrahita et al., "Generation of mice carrying a mutant apolipoprotein E gene inactivated by gene targeting in embryonic stem cells," *Proc. Natl. Acad. Sci. U. S. A.* **89**(10), 4471–4475 (1992).

Sangpil Yoon received his BS and MS degrees in mechanical engineering from Yonsei University, Seoul, Republic of Korea, and in aerospace engineering from Georgia Institute of Technology, Atlanta, Georgia, and his PhD in mechanical engineering from University of Texas at Austin, Austin, Texas, USA, in 2012. He is a postdoctoral fellow at the University of Southern California. His current research interests include intravascular ultrasound imaging system development, acoustic-transfection using high frequency ultrasound, and fundamental research of cell physiology using ultrasound.

Min Gon Kim received his BS degree in electrical engineering from the Kwangwoon University, Seoul, Republic of Korea, in 2009 and his MS degree in electrical engineering from University of Southern California, Los Angeles, California, USA, in 2012. Currently, he is pursuing his PhD in biomedical engineering at the University of Southern California. His research interests include ultrahigh frequency ultrasound front end system and ultrasound microbeam.

Jay A. Williams serves as manager at the NIH Resource on Medical Ultrasonic Transducer Technology. Some of his accomplishments include development of 128-element 25- to 30-MHz composite 30-μm pitch phased arrays, 256-element 30-MHz composite 50-μm pitch linear arrays, 8-element 35- to 60-MHz annular arrays, very lightweight high-frame-rate B-scan transducers. Currently, he holds Patent No. 7695784, covering postpositioning for interdigital bonded composites. He has worked in the ultrasound field for more than 20 years.

Changhan Yoon received his MS and PhD degrees of electronic engineering from Sogang University, Seoul, Korea, in 2009 and 2013, respectively. He is currently a postdoctoral research associate in the NIH Resource Center for Medical Ultrasonic Transducer Technology at the University of Southern California, Los Angeles, California. His main research interests include medical ultrasound and photoacoustic imaging, system, clinical applications, and ultrasound microbeam.

Bong Jin Kang received his MS degree in the Department of Electrical Engineering and Biomedical Engineering from the University of Southern California, Los Angeles, California, USA, in 2008 and 2010, respectively. Currently, he is a PhD candidate in the Department of Biomedical Engineering, University of Southern California, Los Angeles, California, USA. His current research is focused on high-frequency array-based ultrasound imaging system for small animal imaging.

Nestor Cabrera-Munoz obtained his BS degree in mechanical–electrical engineering from Monterrey Institute of Technology (ITESM Campus Monterrey, Mexico) in 2005 and his MS degree in biomedical engineering from the University of Southern California, Los Angeles, California, USA, in 2010. Currently, he is pursuing his PhD in biomedical engineering at the University of Southern California. He is focusing his research on high-frequency ultrasonic transducers and arrays.

K. Kirk Shung is a dean's professor in biomedical engineering at the University of Southern California. He obtained his PhD in electrical engineering from the University of Washington, Seattle, Washington, USA, in 1975. He has been the director of the NIH Resource on Medical Ultrasonic Transducer Technology since 1997. He has published more than 400 papers and book chapters.

Hyung Ham Kim is a sales manager at Analogic Corporation. He received his BS degree in electrical engineering from Korea Advanced Institute of Science and Technology, Daejeon, Republic of Korea, in 1993 and his MS and PhD degrees in biomedical engineering from the University of Southern California, Los Angeles, California, USA, in 2006 and 2010, respectively. His current research interests include the design and fabrication of high-frequency transducers/arrays for high-resolution ultrasound imaging and therapeutic applications.